

Probing the 2-D kinematic structure of early-type galaxies out to 3 effective radii

Robert N. Proctor^{1,2}, Duncan A. Forbes¹, Aaron J. Romanowsky³, Jean P. Brodie³, Jay Strader⁴, Max Spolaor¹, J. Trevor Mendel¹, Lee Spitler¹

¹ Centre for Astrophysics & Supercomputing, Swinburne University, Hawthorn VIC 3122, Australia

² Universidade de São Paulo, IAG, Rua do Mato, 1226, São Paulo, 05508-900, Brazil

³ UCO/Lick Observatory, University of California, Santa Cruz, CA 95064, USA

⁴ Harvard-Smithsonian Centre for Astrophysics, 60 Garden St., Cambridge, MA 02138, USA

Hubble Fellow

Email: rproctor@astro.iag.usp.br, dforbes@astro.swin.edu.au

1 April 2024

ABSTRACT

We detail an innovative new technique for measuring the 2-D velocity moments (rotation velocity, velocity dispersion and Gauss-Hermite coefficients h_3 and h_4) of the stellar populations of galaxy halos using spectra from Keck DEIMOS multi-object spectroscopic observations. The data are used to reconstruct 2-D rotation velocity maps.

Here we present data for five nearby early-type galaxies to 3 effective radii. We provide significant insights into the global kinematic structure of these galaxies, and challenge the accepted morphological classification in several cases. We show that between 1.3 effective radii the velocity dispersion declines very slowly, if at all, in all five galaxies. For the two galaxies with velocity dispersion profiles available from planetary nebulae data we find very good agreement with our stellar profiles. We find a variety of rotation profiles beyond 1 effective radius, i.e. rotation speed remaining constant, decreasing and increasing with radius. These results are of particular importance to studies which attempt to classify galaxies by their kinematic structure within one effective radius, such as the recent definition of fast- and slow-rotator classes by the SAURON project. Our data suggests that the rotator class may change when larger galactocentric radii are probed. This has important implications for dynamical modeling of early-type galaxies. The data from this study are available on-line.

Key words: galaxies: general, galaxies: individual; (NGC 821; NGC 1400; NGC 1407; NGC 2768; NGC 4494), galaxies: kinematics and dynamics, galaxies: structure, stellar dynamics, techniques; spectroscopic,

1 INTRODUCTION

Since the pioneering work of Siskin (1974), major advances in the measurement of stellar orbits in early-type galaxies have been made. The first quantities to be measured were the line-of-sight rotation velocity (V_{rot} ; which can be considered a measure of ordered motion within a galaxy) and velocity dispersion (σ ; a measure of the random motions). By combining these two measures with photometric ellipticity (e) it was possible to probe the anisotropy of stellar orbits in galaxies (Binney 1978).

Further progress was made in this field when, in the 1980s, Bender (1988) showed that although the isophotal

shapes of early-type galaxies were well described by ellipses, small variations from ellipticity could be used to categorise them as either ‘boxy’ or ‘discy’, and that these variations relate directly to the stellar orbital isotropy. The combination of surface photometry and detailed kinematics were therefore demonstrated to provide significant insights into the global structure of galaxies.

More recently, higher order moments of the line-of-sight velocity distribution (LOSVD) have been measured (e.g. Bender 1990; Rix & White 1992; Gerhard 1993; van der Marel & Franx 1993). These characterise deviations from a pure Gaussian shape, e.g. skewed and symmetric deviations, denoted h_3 and h_4 respectively. Such parameters can

indicate kinematic substructures, such as embedded stellar discs.

The development of integral field units (IFUs), such as the SAURON instrument, have given new impetus to this field, as these provide 2-D maps of the LOSVD. This allows the definition and estimation of a number of important new parameters that can be averaged over the surface of a galaxy in a self-consistent way. Perhaps the most important of these is the ‘spin’ parameter (λ_R) which is a proxy for the projected angular momentum per unit mass. Applied to the SAURON galaxy sample of 48 early-type galaxies, it was used to show that a dichotomy exists between ‘slow-’ and ‘fast-’ rotators (Emsellem et al. 2007). Trends between photometric and kinematic axis ratios and position angles have also been shown to vary with λ_R ; with slow-rotators often exhibiting strong misalignments. These observations provide new clues to the formation mechanisms of these differing galaxy types (Krajinovic et al. 2008; Cappellari et al. 2007; Thomas et al. 2007).

Statler & Smecker-Hane (1999) used a different approach to building 2-D maps of the LOSVD in NGC 3379. Using long-slit spectroscopy along four position angles, they were able to reconstruct a model of the 2-D kinematics by making suitable interpolations between their observed axes. However, such studies are rare due to the large amount of telescope time required to observe multiple position angles out to large radii.

Despite these advances, most observations typically reach to less than one effective radius, with only a handful of studies extending this coverage up to $2\text{--}3 R_e$ (but see Saglia et al. 1993; Graham et al. 1998; Mehlert et al. 2000; Proctor et al. 2005; Sanchez-Balazquez et al. 2006; Forestell & Gebhardt 2008). However, such outer regions potentially provide key information regarding the physical properties of galaxies. For example, radii within $1 R_e$ only sample 50% of the baryonic mass and $\sim 10\%$ of the angular momentum of an idealised galaxy with an $R^{1.4}$ like light profile and a flat rotation profile. The situation is even worse when considering the distribution of total galaxy mass (including dark matter). For instance, the simulations of Deke et al. (2005) show that only $\sim 5\%$ of the total mass is contained within $1 R_e$ (see also Mamon & Lokas 2005). Furthermore, the signatures of some formation mechanisms only become apparent at large galactocentric radii (e.g. McDillan, Athanassoula & Dohlen 2007; Weil & Hemsquist 1996). A means to probe the kinematics in the outer regions of early-type galaxies, and hence include a significant fraction of a galaxies’ angular momentum and mass, is therefore highly desirable.

In this paper we measure stellar LOSVDs from deep multi-object spectroscopic observations and develop a new technique for their analysis. Specifically, we measure rotation velocity, velocity dispersion and the Gauss-Hermite coefficients h_3 and h_4 , out to $3 R_e$ in vein nearby early-type galaxies. By extending the region studied to such radii we encompass more than 85% of the baryonic mass, 30% of the angular momentum and 15% of the total mass, a significant increase in the fractions so surveyed in galaxies. To achieve this we exploit the large aperture of the Keck telescope, the high sensitivity of the DEMOS instrument at 8500 Å and the strong calcium triplet absorption features at these wavelengths. Even with this configuration, expo-

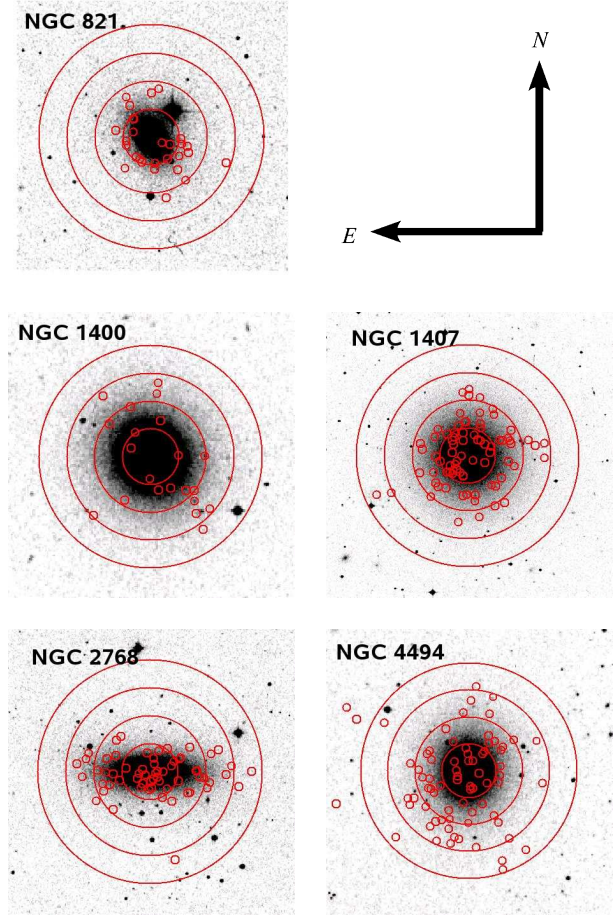


Figure 1. DSS images of the 5 target galaxies. Small red circles mark the location of slits from which galaxy background spectra were obtained. Large red circles represent 1, 2, 3 and 4 effective radii.

surements of ~ 2 hours are required for our analysis.

The paper is organised as follows: In Section 2 we outline the observations and data reductions, detailing the technique by which we extract the host galaxy spectra. In Section 3 we outline our new kinematic analysis technique. Results are presented in Section 4. We discuss our findings in Section 5, and present our conclusions in Section 6.

2 OBSERVATIONS AND DATA REDUCTION

2.1 Sample selection

The galaxies in our sample were selected with the intention of obtaining spectra of their globular clusters (GCs). The galaxies are all nearby, early-types with moderately rich GC systems. The selection also had the requirement that recession velocities were such that the calcium triplet lines would not generally be adversely affected by strong sky lines. The main science goal was to obtain GC kinematics, and hence probe the mass profile of their host galaxy halos. Initial results for NGC 1407 from the 2006 Nov. run have recently been reported in Romanowsky et al. (2008).

2.2 Observations

The data used in this work are from three observing runs using DEIMOS on the Keck-2 telescope. The first observing run was carried out in 2006 Nov. using the 1200 l/m grating centered at 7500 Å and a 1 arcsec slit. This allows coverage of the calcium triplet at 8498, 8542 and 8662 Å at a resolution of 1.5 Å. The second run was carried out in 2007 Nov. and the third in 2008 April, both using the same instrument setup as the first run. Seeing was 0.5 to 0.8 arcsec on all nights. A total of five galaxies were observed (NGC 821, NGC 1400, NGC 1407, NGC 2768 and NGC 4494).

Between two and six independent masks were observed per galaxy and the 16×5 arcmin field-of-view allowed the observation of 80–120 spectra in each mask. However, only 20% of these were at radii from which the signal of the background host galaxy was sufficient for the extraction of spectra (see Table 4).

Fig. 1 shows the positions of slits from which host galaxy spectra were extracted. We note that it was only possible to measure recession velocities in some of the outermost slits, i.e. velocity dispersion and higher order moments are not presented for some of the outermost positions.

2.3 Data reduction

Data reduction were carried out using the DEIMOS DEEP 2 pipeline software. This package produces a variety of outputs from the raw DEIMOS data, including both object and ‘sky’ spectra. The data reported here probe the kinematics of the stellar populations in the galaxy halos. These are based on the ‘sky’ spectra that were subtracted from the globular cluster spectra (the prime targets of the observation, see Romanow sky et al. 2008). The ‘sky’ spectra actually consist of a co-addition of the true sky and the background galaxy light. In order to distinguish them from the true sky spectrum we shall therefore henceforth refer to these as the ‘background’ spectra.

The recovery of the galaxy spectra requires an estimate of the true sky spectrum in each of the background spectra. For each mask, the sky spectra were estimated from the average of four to six of the background spectra sampling large distances from the galaxy centre (see below). These generally lay beyond $6(7 R_e)$. Even at this distance some galaxy light is still present. However, since the data reported here are limited to within $3 R_e$, the galaxy light contamination of the sky estimates constitutes only a small fraction of the galaxy light in our science spectra. Assuming a de Vaucouleur’s (1953) $R^{1.4}$ profile, we estimate that, in points at $3 R_e$, the sky estimate contains only $< 10\%$ of the galaxy light in the science spectra. This falls to 4% at $2 R_e$. Errors caused by the residual galaxy light in our sky estimates are therefore likely to be much smaller than the quoted errors on data points at these radii, which are often as much as 30% of the measured parameter values.

In order to select and characterise the sky spectra, a sky index was defined (see Table 2 and Fig. 2). The central band of this index was defined to cover the strong sky emission lines between 8600 and 8700 Å. The sidebands of the index were chosen to cover regions of the background spectra that were relatively free of both significant sky emission lines and

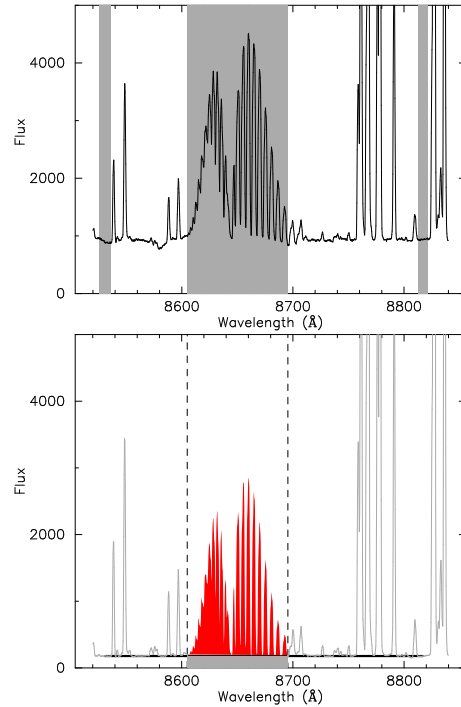


Figure 2. Definition of the sky index. Upper plot shows wavelength regions of the two sidebands and the central band in a spectrum with significant galaxy halo signal. Lower plot shows the region used in the calculation of the sky index in a scaled sky spectrum. The index is defined as a ratio, i.e. excess flux in the central band (counts in shown in red) divided by continuum flux (counts shown in grey).

galaxy absorption features. For each background spectrum the sky index was then calculated as follows: First, the continuum level in the region of the central band was estimated by integrating under the linear interpolation of the average fluxes in the sidebands. Then the excess flux in the central band was calculated as the total flux in the region minus the integrated continuum flux. Finally, the sky index was calculated as the ratio of the excess central band flux to its continuum flux (see Fig. 2; bottom). The index has the property that, as one moves away from the galaxy centre (and the galaxy light contribution to the background spectrum decreases), the index tends to a constant value (see Fig. 3). After a careful visual inspection of the spectra, the background spectra to be used as sky estimates were selected from this constant region. These were co-added to provide a higher signal-to-noise estimate of the sky spectrum.

The index was used to select candidate sky spectra, rather than simply choosing the slits at the greatest distance from the galaxy centre, as the index allows identification of spectra suffering from reduction problems not detected by visual inspection. For the most part, these proved to be either slits located near the edges of the mask where vignetting effects are large, or slits in which residual globular cluster light was still present. Fig. 3 illustrates how the sky index allows identification (and elimination) of slits with such problems.

Sky subtraction was carried out by consideration of the excess flux in the central band as defined above. First, for each background spectrum, we scaled the sky estimate such

Galaxy	Hubble Type	Distance (Mpc)	R_e (arcsec)	M_K (mag)	PA_{phot} ($^\circ$)	Axis ratio (K band)	V_{sys} (km s^{-1})
NGC 821	E6?	22.4	50	-23.6	30	0.62	1729
NGC 1400	SA0-	25.7	29	-23.8	35	0.90	574
NGC 1407	E0	25.7	70	-24.9	60	0.95	1782
NGC 2768	S0 ₁₌₂	20.8	64	-24.6	93	0.46	1327
NGC 4494	E1{2	15.8	49	-24.8	173	0.87	1335

Table 1. Properties of galaxies featured in this work. Distances are from surface brightness fluctuations by Tonry et al. (2001), with the distance modulated by 0.16 according to Jensen et al. (2003). The values for NGC 1400 and NGC 1407 are taken as the average of their individual values. Hubble types are from NED and effective radii are from RC3. Absolute K band magnitudes are calculated from 2MASX apparent magnitudes and the distances given in column 3. Photometric position angles (PA_{phot}) and K band photometric axis ratios are from 2MASX. Systemic velocities are the values derived from our fitting of central data points (see Section 4).

Band	Wavelengths
Sideband 1	8526.0 { 8536.0 Å
Central band	8605.0 { 8695.5 Å
Sideband 2	8813.0 { 8822.0 Å

Table 2. Band definitions for the sky index used in the selection and subtraction of sky spectra.

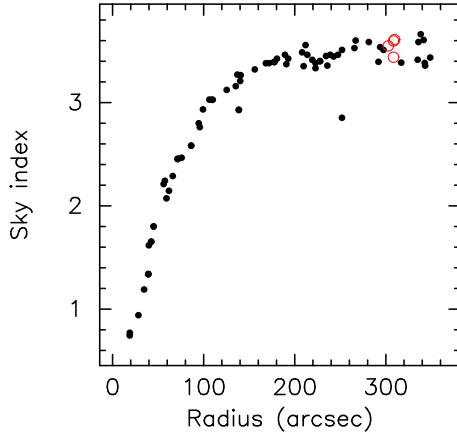


Figure 3. Sky index with radius for one set of NGC 4494 observations. Open red circles represent points whose spectra were co-added to generate the sky spectrum. Two points clearly exhibit aberrant behavior. These are not included in the final sample.

that the resultant spectrum had the same excess counts as the target spectrum. Subtraction of the scaled sky spectrum therefore resulted in a spectrum with no excess counts in the sky band region, i.e. with counts in the sky band region equal to the continuum level in the sidebands. This method provides a sky subtraction accurate to approximately one count over the sky band region. We show examples of sky subtracted spectra in Fig. 4 in which it can be seen that although sky residuals are present, these are not significantly larger than the Poisson noise associated with the strong sky-lines. Assuming a dark-sky brightness at Muna Kea of $I = 20 \text{ mag. arcsec}^{-2}$, then our galaxy halo spectra can reach as low as 1{10% of the sky background. We note that this sky subtraction technique is similar to that used in Proctor et al. (2008) and Norris et al. (2008) in the analysis of optical spectra from GEMINI/GMOS.

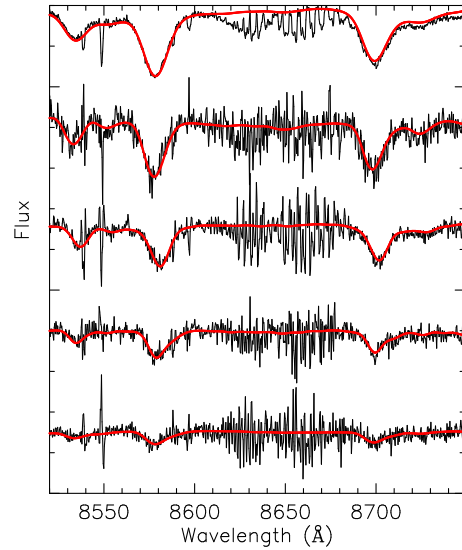


Figure 4. Sky subtracted spectra of NGC 2768. Red lines show the best-fit template derived by the pPXF code during measurement of velocity moments. Spectra are in order of decreasing signal-to-noise broadly covering the range within our data (from 40 in the top spectrum down to 7 in the bottom spectrum).

3 ANALYSIS METHOD

The analysis presented here involves measurement of velocity moments (V , and the Gauss-Hermite coefficients h_3 and h_4) using the pPXF code of Cappellari & Emsellem (2004) – an extension of the pixel fitting code of van der Marel (1994).

3.1 Measurement of kinematics

The pPXF software works in pixel space, finding the combination of template stars which, when convolved with an appropriate line-of-sight velocity distribution, best reproduces the galaxy spectrum. Thirteen template stars were used, ranging in spectral type from F8 to M1. This method of kinematic analysis has the advantage that template-mismatch issues are all but eliminated. Operating in pixel space, the code also permits the masking out of regions of the galaxy spectrum during the measurement. This is of particular importance in our data as, despite the accurate sky subtraction, the spectra still suffer from skyline residuals (see Fig.

4). The code also allows suppression of the higher order moments h_3 and h_4 (i.e. fitting only V_{obs} and σ). This was found to be useful in order to stabilise the fits in low signal-to-noise spectra.

Errors were estimated from a repeat observation on different nights of one of the masks of NGC 2768. By binning the 60 repeat measurements by observed signal (i.e. counts), the rms variations of each of the velocity moments in the repeat measurements were calculated as a function of signal-to-noise. The trend of rms with signal-to-noise so obtained was then used to make estimates of errors in this, and other galaxies.

As a test of the accuracy of our measurements we compared them to those of SAURON (Emmelman et al. 2004) for the two galaxies in common between the studies. This was possible as our data samples 10 precise locations (9 in NGC 2768 and one in NGC 821) that are also sampled by SAURON. The results of the comparison for σ and h_3 are shown in Fig. 5. A small systematic offset of $\{12.9 \text{ km s}^{-1}$ is evident in our velocity dispersion data compared to the SAURON values, with a scatter of 7.3 km s^{-1} . The measured h_3 values are consistent within their errors. We do not compare h_4 , as errors are generally large with respect to our measured values. We leave comparison of V_{obs} to the sections presenting our results.

During the analysis significant discrepancies were detected between our results for the values of NGC 1400 and NGC 1407 and the long-slit data of Spolaor et al. (2008a). As a consequence, the data of Spolaor et al. (2008a) were re-processed through the pPXF software using a large number of template stars, resulting in significantly improved measurements (see Appendix A).

The measured velocity moments of all the galaxies are available on-line. An example of the available data are presented in Table 3.

3.2 Kinematics

Our analysis of these data proceeds by consideration of the velocity moments in the space of galacto-centric radius and position angle (PA; defined as the angle between the point in the galaxy and the galaxy centre from North through East). For the analysis, the data were binned in radial ranges (i.e. circular shells) for comparison to the expectations for rotating isotropic ellipsoids (or, equivalently, inclined discs). Fits of the observed velocity (V_{obs}) data were carried out by least-squares minimisation of the data to the equation:

$$V_{\text{obs}} = V_{\text{sys}} + V_{\text{rot}} \cos(\theta); \quad (1)$$

where V_{sys} is the systemic velocity of the system, V_{rot} is the major-axis rotation velocity and θ is defined by;

$$\tan(\theta) = \frac{\tan(\text{PA} - \text{PA}_{\text{kin}})}{q}; \quad (2)$$

with PA_{kin} the position angle of the major rotation axis and q the rotation axis-ratio. The values of V_{rot} , PA_{kin} and q were all allowed to vary freely. Values of V_{sys} were taken as the value derived from the high-signal-to-noise data of our innermost points (i.e. generally the points within $1 R_e$). This value was then assumed for all radial bins.

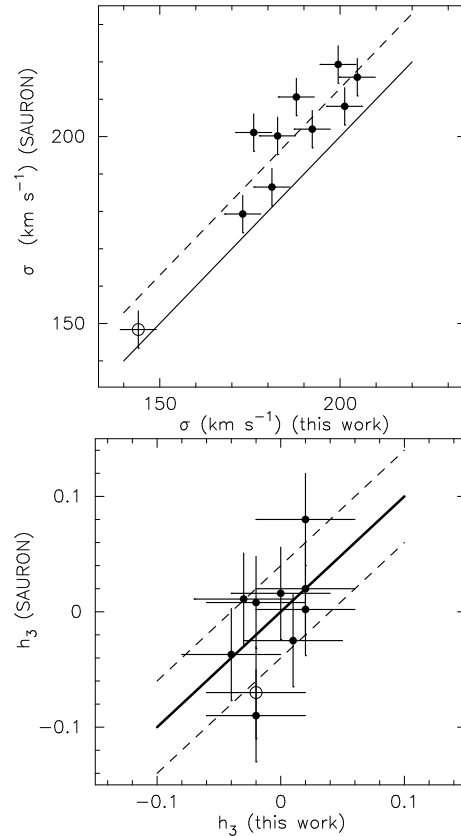


Figure 5. Comparison of velocity dispersion measures (top) and h_3 (bottom) with SAURON data (Emmelman et al. 2004). Filled symbols are from NGC 2768, and the open symbol from NGC 821. In the plot of σ , the one-to-one (solid) and $\{12.9 \text{ km s}^{-1}$ offset (dashed) lines are shown. In the plot of h_3 the one-to-one line (solid) and typical errors (dashed) of 0.04 are shown.

In the analysis of the rotation properties of our sample galaxies we used two types of radial binning. The first was to break the data into 2 or 3 independent radial slices (i.e. into circular annuli), the other was to carry out rolling fits again with data binned in circular annuli. Results are presented as the major axis values with radii expressed in terms of the effective radius (R_e)¹. Errors on these fits were estimated as the rms scatter in the results of 50 Monte Carlo simulations of the data using the best-fit parameter values and scatter.

We were not however able to carry out such an analysis on the velocity dispersion data, mainly because we detect little to no variation in this parameter over the radii probed by our data. We are therefore not able to measure the axis ratio of this velocity moment. However, for two galaxies (NGC 821 and NGC 2768), the SAURON data of Emmelman et al. 2004 permit estimation of axis ratios of q in the inner regions. For NGC 821 the SAURON data appear to show an axis ratio close to 1.0 (despite the ellipticity of the galaxy isophotes). On the other hand, in NGC 2768 q appears to have a simi-

¹ Note that R_e is expressed as the radius of a circle with the same area as the ellipse encompassing 50% of the galaxy light. Therefore, in galaxies with non-zero ellipticity, a point on the major axis at $1 R_e$ does not lie on, but rather within, the half-light ellipse.

R.A.	Dec.	V_{obs}	V_{obs} error	error	h_3	h_3 error	h_4	h_4 error	
NGC 2768									
9:11:31.97	+60:1:38.7	1300	26	152	24	0.14	0.04	0.10	0.05
9:11:28.47	+60:2:51.5	1251	27	177	25	0.05	0.04	0.03	0.05
9:11:35.29	+60:2:03.8	1284	5	192	4	0.02	0.04	0.02	0.05
9:11:38.70	+60:2:57.4	1346	26	154	24	-0.02	0.04	-0.01	0.05
.....

Table 3. Example of the velocity moment data from this work. Columns are; R.A. and Dec (J2000), observed recession velocity (V_{obs} in km s^{-1}), velocity dispersion (in km s^{-1}) and Gauss-Hermite coefficients h_3 and h_4 . The full table is available on-line.

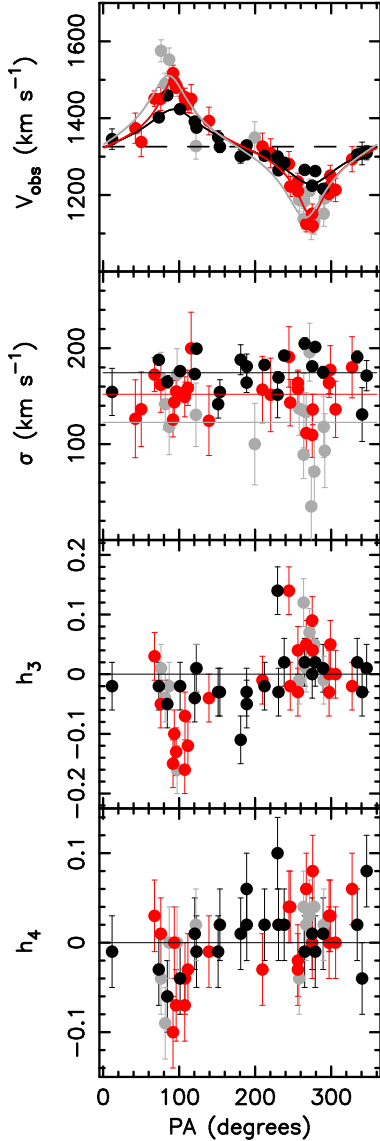


Figure 6. NGC 2768. Velocity moments are plotted against position angle. Data points are coloured according to galactocentric radius (black; $R < 1 R_e$, red; $1 R_e < R < 2 R_e$ and grey; $R > 2 R_e$). In the plot of V_{obs} best-fit elliptical models at each radius are shown as appropriately coloured lines. The systemic velocity (V_{sys}) is shown as a dashed line. The major kinematic axis (PA_{kin}) is at 90° . In the plot of average values are also shown as appropriately coloured lines. The values adopted for these lines are presented in Table 4.

lar axis ratio to the isophotes. We therefore adopt these axis ratios for the analysis of the velocity dispersion data from these galaxies. For the remaining three galaxies (all of which have axis ratios > 0.8 we assume an axis ratio of 1.0.

We also experimented with the co-adding of spectra at similar effective radii for measurement. However, this process requires the spectra to be de-redshifted prior to co-addition, which complicates the handling of the sky-line residuals in the absorption features. In addition the results proved almost identical to the values obtained by averaging individual measurements. On the basis that simplest is best, we therefore present values as individual and radially averaged values.

Our analysis is similar in intent to the ‘kinemetry’ of the SAURON paper by Krajnovic et al. (2006). However, our data possess an extremely low sampling density (i.e. we have on average 60 points inside an area of $24 R_e^2$ compared to SAURON’s 3000 points inside $0.4 R_e^2$ – a data density contrast of 3000:1). Our data are also generally of lower signal-to-noise than the SAURON data. Since, as noted in Krajnovic et al. (2006), such limitations make it impossible to perform a full harmonic analysis, we have restricted our analysis to only the low order harmonics and fitted our data on circles (or more precisely on annuli) rather than ellipses. Unable to perform the full analysis, we have also refrained from adopting the full notation used by Krajnovic et al. (2006). However we note that the rotation velocity (V_{rot}) we report is most directly related to their k_1 parameter, while the kinematic axis ratio is most directly related to their q_{kin} parameter. PA_{kin} has the same meaning in both studies.

4 RESULTS

In this section we present the results of our velocity moment measurements (V_{obs} , σ , h_3 and h_4). Errors on individual data points were derived from the repeat measurement of one mask in NGC 2768 (see Section 3). Errors on rolling fits were estimated by Monte Carlo realisations of the best-fit parameters. Note that, for the lowest signal-to-noise spectra, the higher order moments were either suppressed altogether or are not presented. Tests on the low signal to noise spectra show that changes in recession velocity and velocity dispersion caused by the suppression of the h_3 and h_4 parameters are $\sim 20\%$ of the quoted errors. We also present re-constructions of 2-D rotation velocity maps in this section.

The results of the fits to independent radial slices are presented in Table 4. In NGC 821 and NGC 1400 two radial ranges were defined (NGC 821: $R < 1.0 R_e$ and

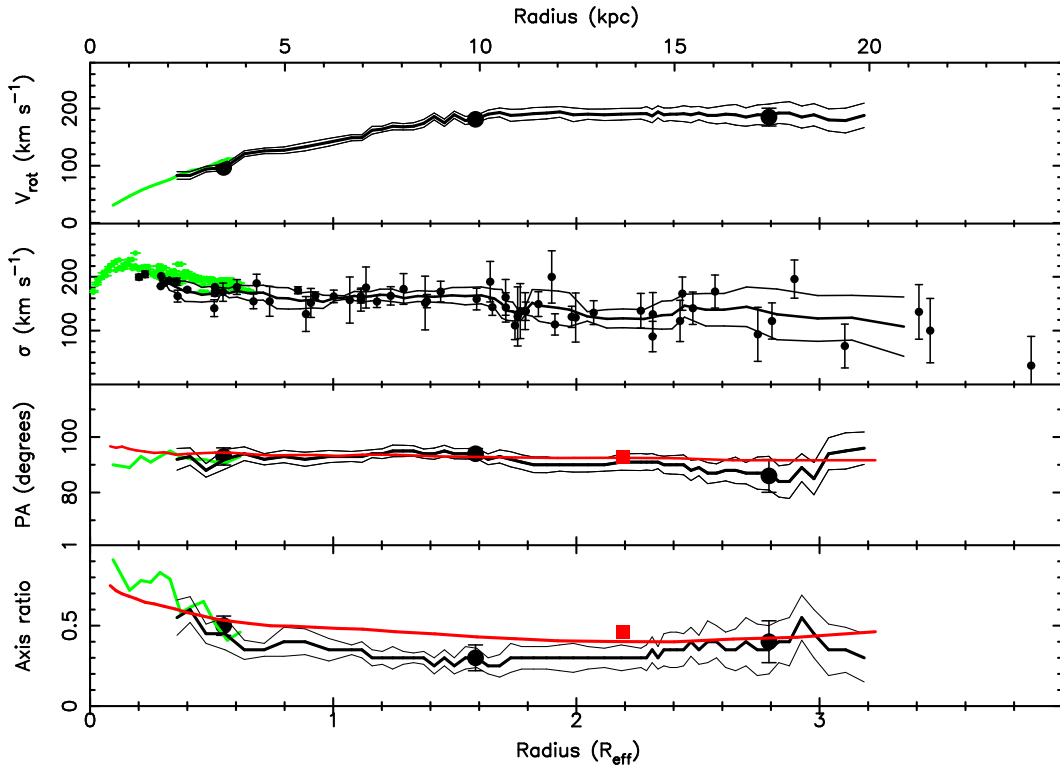


Figure 7. NGC 2768. Radial profiles of the major axis rotation velocity (V_{rot}), kinematic and photometric PA (PA_{kin} and PA_{phot}) and axis ratio (q and $1-q$). Note that ellipticity of q is assumed to be 0.54, i.e. the photometric ellipticity. The physical radial distances (based on data in Table 1) are given in kiloparsec on the top axis. The data points (black) are the individual measured values, with the line representing a rolling average of 5 points. For all other parameters the black data points represent the values of our fits to independent regions (Table 4). The results of rolling fits to the data and their $1-\sigma$ errors are indicated as black lines. Green data points and lines at small radii are from our analysis of the SAURON data of Emsellem et al. 2004. The red squares in PA and axis ratio are the 2MASS photometric values at the radius of the K band 20th magnitude isophote, while the red lines show the R band photometric data of Peletier et al. (1990). Overall the agreement with the literature values is very good.

Galaxy	No	$\langle R \rangle$ (arcsec)	$\langle R/R_e \rangle$ (R_e)	$\langle \sigma \rangle$ (km s^{-1})	V_{rot} (km s^{-1})	axis ratio (q)	PA_{kin} ($^\circ$)
NGC 2768	21	31	0.48	174.4	98.3	0.45 0.06	90.3
	26	93	1.45	152.4	178.6	0.30 0.08	94.2
	15	165	2.57	123.10	190.16	0.35 0.13	88.6
NGC 4494	19	32	0.65	133.3	58.2	0.80 0.03	182.1
	30	75	1.53	111.3	52.3	0.50 0.09	179.3
	33	143	2.91	100.5	54.5	0.40 0.20	170.6
NGC 1407	28	49	0.70	261.6	28.4	(0.95)	254.8
	39	102	1.46	240.7	21.6	(0.95)	245.14
	14	173	2.48	198.11	20.10	(0.95)	248.15
NGC 1400	7	31	1.07	116.3	53.3	(0.9)	34.4
	14	68	2.35	96.7	30.7	(0.9)	40.14
NGC 821	14	41	0.82	149.5	56.8	0.30	33
	17	78	1.56	144.6	6.8	(0.30)	(33)

Table 4. Kinematic data summary for independent radial slices. The definition of the radial binning is outlined in Section 4. The number of slits in each radial bin, their average radius and σ are given as well as the results of the rotation velocity fits (Equations 1 & 2). Data in brackets are assumed (rather than fitted) values.

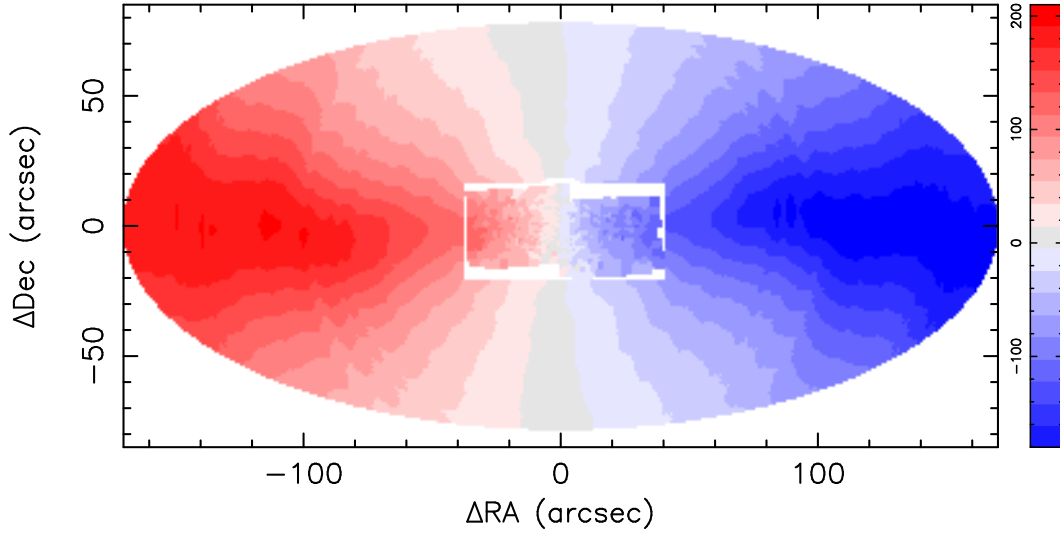


Figure 8. NGC 2768. Reconstruction of the 2-D rotation velocity map using the rolling fits of Fig. 7. The outer boundary of the map has been chosen to reflect the photometric axis ratio of the galaxy (0.46). The colour scale (in km s^{-1}) is shown on the right. A box shown is the SAURON (Emmellem et al. 2004) velocity map of the central regions of the galaxy. The agreement between the data sets is extremely good.

$R < 1.0 R_e$, NGC 1400: $R < 1.5 R_e$ and $R < 1.5 R_e$). In the other three galaxies three ranges were defined ($R < 1.0 R_e$, $1.0 R_e < R < 2.0 R_e$ and $R > 2.0 R_e$).

We first present our results for NGC 2768, as this galaxy possesses high signal-to-noise data, a large sample size, and is also one of the galaxies observed by SAURON.

4.1 NGC 2768

The brightest galaxy in a loose group, NGC 2768 is classified as an E6 galaxy in RC3 (de Vaucouleurs et al. 1991). However, in both the Revised Shapley (Ames Catalogue of Bright Galaxies (Sandage, Tammann & van den Bergh 1981) and the Carnegie Atlas of Galaxies (Sandage & Bedke 1994) it is classified as an $S0_{1=2}$ due to a 'bluish outer envelope'. The galaxy is highly elliptical with K band photometric axis ratio of 0.46, and PA of 93 (Jarrett et al. 2000). It also reveals a polar orbiting dust and gas ring, possibly of external accretion origin (see Martellet al. 2004 and references therein).

Photometric profiles out to 200 arcsec are presented in Pelletier et al. (1990). They find a rapidly rising ellipticity profile with radius (i.e. a falling axis ratio), and report indications of a 'disk-like component' at about 50 arcsec which gives way to boxy isophotes beyond about 100 arcsec.

Fried & Illingworth (1994) probed the kinematics along the minor and major axes out to about 50 arcsec. They found evidence for stellar rotation aligned along the photometric major axis and a 'spheroidal' velocity field. They also detected minor axis rotation associated with the polar ring.

The central regions (80×40 arcsec) of the galaxy were also observed with the SAURON integral field unit (Emmellem et al. 2004). The SAURON results show strong rotation with a 'cylindrical velocity field' and a central dip in (McDermid et al. 2006). They find the galaxy to be a fast-rotator, but, contrary to Sandage & Bedke (1994), conclude that the galaxy '...does not have evidence for a disc'. They

therefore adopt the RC3 classification of this galaxy as an E6.

The SAURON team also investigated the very central regions (4×4 arcsec) using the OASIS integral field spectrograph (McDermid et al. 2006), identifying emission associated with the polar disk and a young (2.5 Gyr) central stellar population. However, other spectroscopic age determinations in the literature generally prove inconsistent, with studies reporting the central stellar population to be both old and young (e.g. Howell 2005; Denicolo et al. 2005; Silchenko 2006). It is unclear whether this reflects inconsistencies in the determination of the properties of the central populations, or is rather a real effect, perhaps caused by variable sampling of the central star-forming disk.

Hakobyan et al. (2008) suggest this galaxy may be a merger remnant with the presence of a young stellar population suggested by '...the existence of strong H I and CO emission, and the presence of dust and ionised gas...'. The recent type Ib supernova SN 2000ds (Filippenko & Chomock 2000) supports this conclusion.

Presenting our results, we first consider the distribution of the NGC 2768 velocity moments with PA. Results are plotted in Fig. 6 with point colour depicting galacto-centric radius. Values derived for each radial bin are presented in Table 4.

The rotation in this galaxy can be seen to be strongly elliptical. An increasing rotation velocity with radius is also evident. The h_3 parameter reflects this behaviour, with near-zero values in the slowly rotating inner regions ($R < 1 R_e$). However, at larger radii h_3 increasingly mirrors the elliptical rotation curve. The increasing signal in h_3 with radius is also detected in the SAURON maps of the galaxy (Emmellem et al. 2004).

Both h_3 and h_4 , however, exhibit unusual behaviour, as they do not possess the minor-axis symmetry expected from even moments (see Krajnovic et al. 2008). This must be

understood in terms of the degeneracy between h_3 and h_4 discussed at length in Cappellari & Emsellem (2004). The degeneracy is worst when; i) signal-to-noise is low, and ii) when two distinct kinematic components have roughly equal luminosities. To test that this was indeed causing the lack of axis-symmetry in our data, we re-fitted the data for this galaxy using pPXF with h_3 and h_4 suppressed (i.e. set to zero). The test confirmed that, if h_4 is forced to zero, the dip in V_{rot} becomes visible on both sides of the galaxy.

Given that the h_4 parameter is more prone to the effects of low signal-to-noise and sky-line residuals than h_3 , we conclude that, in its outer reaches, this galaxy probably exhibits a significant drop in V_{rot} on both sides of the major axis, as would be expected from the disc of an S0 galaxy.

Velocity dispersion appears to be decreasing with increasing radius (Fig. 6 and Table 4). However, the dip on the major axis (PA $\approx 270^\circ$) is clearly affecting measured average values, particularly since the slits in the outer regions of the galaxy from which we were able to recover a galaxy spectrum tend to lie along the major axis where the galaxy light is brightest (Fig. 6). The gradient in V_{rot} presented here may therefore be somewhat exaggerated by this effect. We note for future reference that the four data points with $V_{rot} < 100 \text{ km s}^{-1}$ all lie very close to the major rotation velocity axis.

To measure variations with radius we carried out a rolling fit to the recession velocity data in annuli at increasing radii allowing V_{rot} , PA_{kin} and kinematic axis ratio (q in Equation 2) to vary with radius. The fits were performed using a minimum of 10 data points, increasing to 20 in the outer regions. Results of these fits are presented in Fig. 7. We also performed rolling fits to the SAURON data (Emsellem et al. 2004) for comparison.

The agreement in V_{rot} between our results and the SAURON data is good, with near identical rotation velocities over the whole 20 arcsec overlap region. However, the rotation velocity clearly continues to rise beyond the extent of the SAURON data, with the rotation velocity doubling to 200 km s^{-1} between 1 and $3 R_e$. This has a significant impact on the value of V_{rot}/σ obtained for this galaxy, underlining the importance of data at large radii in the construction of even simple kinematic descriptions of galaxies (see Section 5).

Also shown in Fig. 7 is a plot of q with radius. In this plot the agreement between the SAURON results (Emsellem et al. 2004) and ours can be seen to be reasonable. However, the comparison of q presented in Fig. 5 is largely based on data from this galaxy, and exhibits a 13 km s^{-1} systematic offset. The results indicate a strong radial trend in q within $1 R_e$, which levels off somewhat beyond. However, we again note the increasing tendency for our outer data points to lie along the major kinematic axis and the trend for such points to possess depressed q . To get some idea of the impact these trends might have on our results, consider the four points with the lowest V_{rot} ($< 100 \text{ km s}^{-1}$), which, as noted in the previous section, all lie very close to the major kinematic axis. If these points are excluded from our considerations we would conclude that q was flat beyond $1 R_e$.

We detect a PA_{kin} of 91.3° throughout the galaxy in good agreement with the photometric PA from 2MASS (Jarrett et al. 2000) and Peletier et al. (1990). We detect no variation in PA_{kin} with radius, with our measurements of the SAURON data yielding the same, near-constant value.

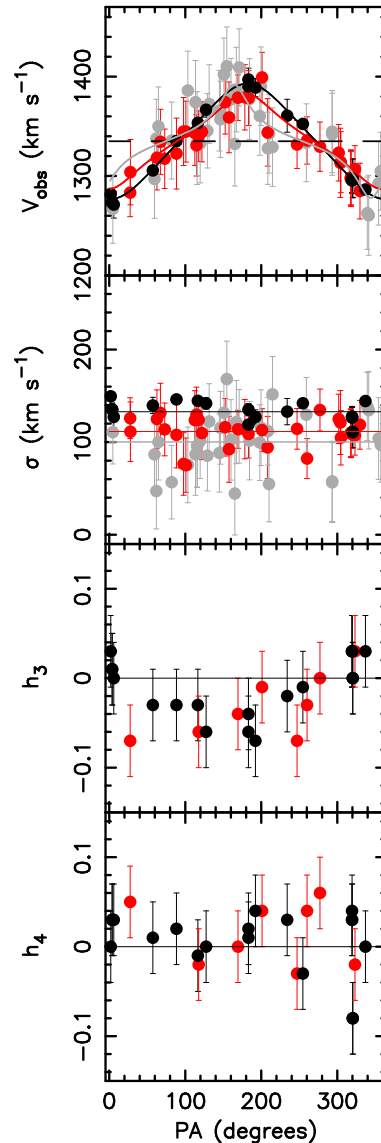


Figure 9. NGC 4494. Same as Fig. 6. The major axis PA is 173° .

Comparison of our rotation axis ratio measurements to those of SAURON again give good agreement in the overlap region. The results clearly indicate that the rotation in the central regions, variously described as ‘cylindrical’ (Emsellem et al. 2004) or ‘spherical’ (Fried & Illingworth 1994), rapidly give way to much more disk-like values at larger radii. Interestingly, the comparison with the photometric axis ratios of 2MASS and Peletier et al. (1990) show the rotation axis ratio to pass from less than the photometric axis ratio in the outer regions to greater than the photometric axis ratio in the inner regions. The most natural explanation for the galaxy having a smaller photometric than kinematic axis ratio in the inner regions is the presence of a highly inclined, but inclined disc, such as would be found in an S0 galaxy, in accord with the Sandage et al. (1981) and Sandage & Bedke (1994) classifications.

To aid in the visualisation of our results, and to facilitate the comparison of our results with those of SAURON, we have reconstructed the 2-D velocity map of NGC 2768 in

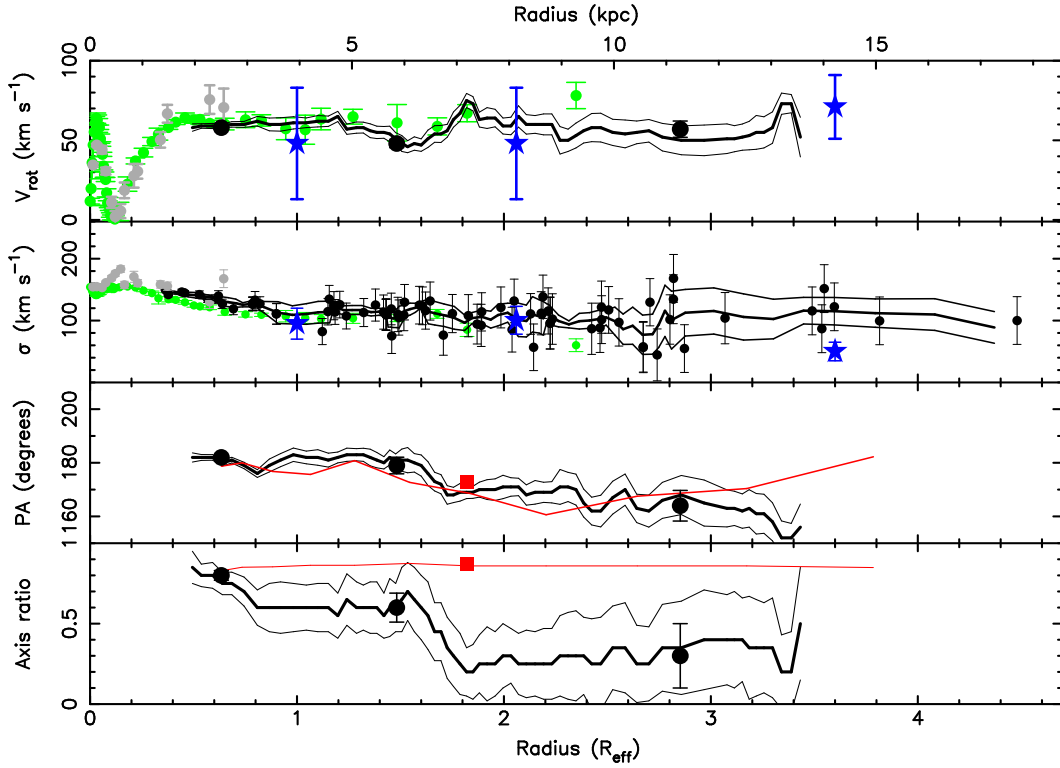


Figure 10. NGC 4494. Same as Fig. 7 with the following exceptions. Green data points in V_{rot} and σ plots are the major axis data from Napolitano et al. (2009). The planetary nebula data (blue stars) are also from Napolitano et al. (2009). Grey data points are the data of Bender, Saglia & Gebhardt (1994). Red lines in plots of PA and axis ratio are the V band results of Napolitano et al. (2009). Large o sets between the kinematic and photometric axis ratio and position angles can be seen.

Fig. 8. The image was generated using the rolling fits values of V_{rot} , PA_{kin} and rotation axis ratio of Fig. 7. A green tint with the SAURON results can be seen to be extremely good. Also evident is the progression from ‘cylindrical’ rotation in the inner, bulge dominated regions to discy rotation in the outer regions probed by our data.

In summary, our results for this galaxy are all in accord with the Shapley (A mes C catalogue (Sandage et al. 1981) and Carnegie Atlas of Galaxies (Sandage & Bedke 1994) classifications of this galaxy as an S0, with the disk-like kinematics in the outer regions giving way to the more ‘cylindrical’ rotation in the inner regions.

4.2 NGC 4494

NGC 4494 is an elliptical galaxy in the Coma I cloud (Forbes et al. 1996) with a K band photometric position angle of 173 and axis ratio of 0.87 (Jarret et al. 2000). It reveals a small central dust ring with 60 degree inclination (photometric axis ratio 0.5) aligned with the major axis of the galaxy (Carollo et al. 1997). The central regions also host a kinematically distinct core (Bender 1988). The mass modeling analysis of Kronawitter et al. (2000) indicates a rising M/L profile. However, evidence for dark matter in NGC 4494 has been questioned by Romonow sky et al. (2003) based on an extended profile from planetary nebulae kinematics (but see also Dekel et al. 2005 and Napolitano et al. 2009). The stellar population analysis of Denicob et al. (2005) found an intermediate age of 6.7 Gyr in the central

regions, indicating that this is not a simple, old, passively evolving elliptical galaxy.

Our analysis of this galaxy was the same as that for NGC 2768. The distribution of the velocity moments with PA are shown in Fig. 9. Results show the rotation in this galaxy to be strongly elliptical, but rotation velocity shows no sign of variation with radius. Within $1 R_e$, the h_3 parameter shows the anti-correlation with V_{rot} expected from a disc embedded in a more slowly rotating (or non-rotating) bulge, although it is not possible to trace this behaviour out to the outer regions where the signal-to-noise is low. We find a decreasing h_3 with radius which attens out beyond $1 R_e$. We find no evidence for variation of h_3 with PA.

The rolling fits to V_{obs} are presented in Fig 10. These fits were performed using 10 data points in the inner region rising to 20 data points in the outer regions of the galaxy. For V_{rot} , we find good agreement with profiles in the literature. Our results are also consistent with the planetary nebulae data of Napolitano et al. (2009) in the outer regions (notwithstanding their large uncertainties). As deduced from Fig. 9, the galaxy exhibits no sign of variation in rotation speed with radius over the whole radial range from $1/3 R_e$. The reconstructed 2-D velocity map of this galaxy is shown in Fig. 11.

Agreements with the profiles and planetary nebulae data in the literature are again good, with declining steadily with radius within $1 R_e$, but leveling off beyond. Indeed, beyond $1 R_e$, the data are consistent with no slope in h_3 at the 1- σ confidence level.

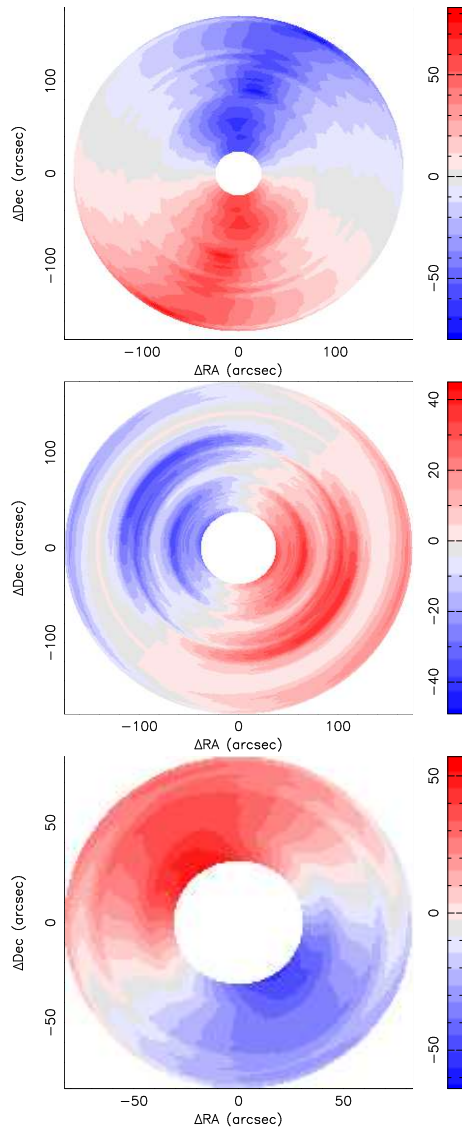


Figure 11. Reconstructed 2-D velocity maps of (top to bottom) NGC 4494, NGC 1407 and NGC 1400. Colour scales (in km s^{-1}) are shown to the right of each image. Note that the variations in V_{rot} with radius in NGC 1407 that causes the unusual patterning in the reconstruction are only detected at 1- σ significance.

The kinematic position angle exhibits a shift of $\sim 10^\circ$ at $1.5 R_e$, mirroring the shift in photometric position angle (Napolitano et al. 2009).

The rotation axis ratio is similar to the photometric axis ratio in the innermost regions, but falls rapidly at the radius at which the position angle changes. The photometric axis ratio (Napolitano et al. 2009), on the other hand, remains near constant with radius. The disparity in axis ratios is all the more curious when the lack of photometric evidence for an embedded disc at these radii (Carollo et al. 1997) is considered. However, it is interesting to note that the kinematic axis ratio in the outer regions of the galaxy is similar to the photometric axis ratio of the central embedded disc of ~ 0.5 (Carollo et al. 1997). This suggests that the inner disc could in fact be part of a much larger (warped) disc structure.

The interpretation of the kinematics in this galaxy is

clearly complex. The highly elliptical V_{rot} and h_3 at $1 R_e$ and their possible association with the central disc would seem to suggest that this galaxy harbours an embedded stellar disc at large radii. However, the lack of photometric evidence for such a disc raises serious questions about such an interpretation. An alternative description is suggested by the results of Balcells (1991) who shows that the signature of rotation accompanied by an h_3 signal can be generated by a minor merger event, as a result of the re-distribution of the angular momentum of the merging galaxy. Such an event could also be responsible for the shift in photometric and kinematic position angles at $1.5 R_e$. Our results are therefore at least qualitatively consistent with the idea that this galaxy is a merger remnant. The presence of a kinematically distinct core (Bender 1988) also supports this interpretation.

4.3 NGC 1407

NGC 1407 is the brightest group galaxy in a dwarf galaxy dominated group (Trentham et al. 2006). The galaxy has been classified as a weakly rotating E0 (Longo et al. 1994) with a "core-like" central luminosity profile (Lauer et al. 1995; Spolaor et al. 2008a). The stellar population analysis of Spolaor et al. (2008b) found the galaxy to possess a uniformly old age within $0.6 R_e$.

Plots of velocity moments with PA are presented in Figure 12. The data were not fitted for kinematic axis ratio due to low signal-to-noise and the large uncertainties in its axis ratio when the value approaches 1.0. However, it is clear from the plot of V_{obs} with PA that the rotation has very low ellipticity (kinematic axis ratio ~ 1.0), similar to the 2MASS photometric axis ratio of 0.95. This value was therefore assumed for the rolling tests. A slow ($\sim 25 \text{ km s}^{-1}$) rotation is evident in all three radial bins. There is a suggestion of non-zero h_3 in the inner regions, consistent with the results of the re-analysis of Spolaor et al. (2008a) data (see Appendix A). The data suggest a declining h_3 with radius.

Rolling tests were performed on the V_{obs} data using 12 data points in the inner region rising to 20 data points in the outer regions of the galaxy (Figure 13). The results confirm the near constant V_{rot} with radius between 0.5 and $3 R_e$ (we note that the variations with radius are only of order 1- σ significance). Figure 13 also confirms the shallow decline in h_3 with radius identified above. The reconstructed 2-D velocity map of this galaxy is shown in Figure 11.

PA_{kin} shows a 2σ deviation from the photometric PA of Goudfrooij et al. (1994) in the inner regions ($< 1.0 R_e$), but is in good agreement with the 2MASS photometric PA at $1.5 R_e$. The cause of the apparent discrepancy in the inner regions is unclear, although significant triaxiality is one possible cause. However, it may also simply be the result of the large uncertainties that arise when fitting both photometric and kinematic data when axis ratios approach unity.

4.4 NGC 1400

Variously classified as an E (e.g. da Costa et al. 1998) and an S0 (e.g. 2MASS; Jarrett et al. 2003), this galaxy is associated, but apparently not interacting with, the NGC 1407

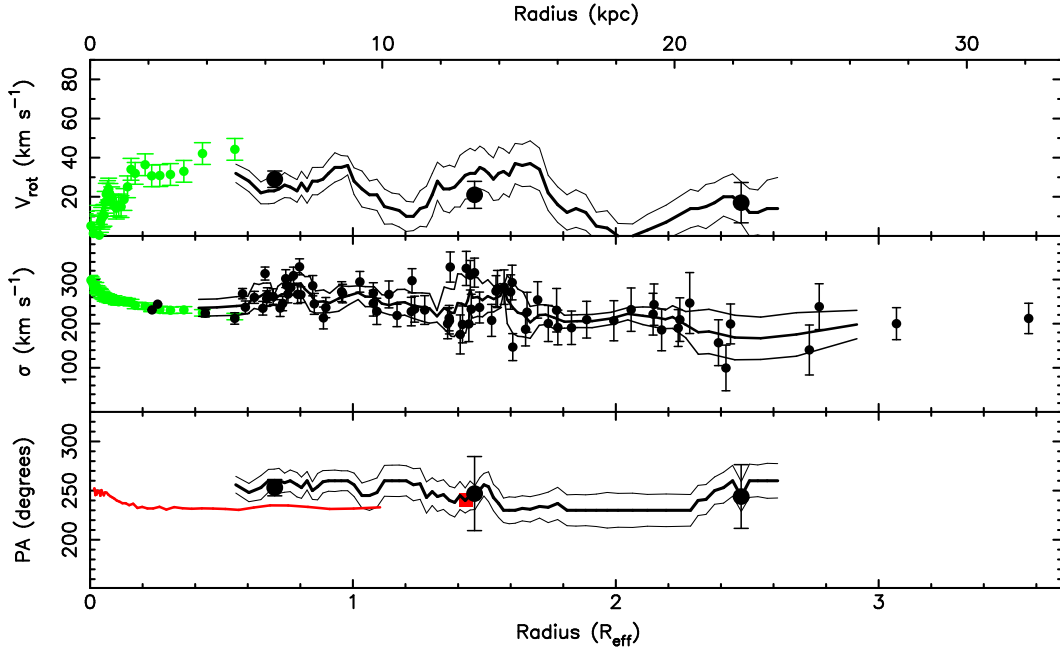


Figure 13. NGC 1407. Same as Fig. 6 with the following exceptions. Kinematic axis ratio is not presented as the proximity of the rotation axis ratio to 1.0 makes its constraint beyond the capabilities of the signal-to-noise of our data. In the V_{rot} and σ plots green points are from our re-measurement of the data of Spolaor et al. (2008a) (see Appendix A). The red line in the PA plot is the I band data of Goudfrooij et al. (1994). Photometric PAs are shown with a 180 degree offset for the purpose of comparison to the kinematic data.

group. Spolaor et al. (2008b) found the stellar population to possess a uniformly old age out to $1.3 R_e$.

The distribution of V_{obs} and σ with PA are shown in Fig. 14. As for NGC 1407, the kinematic axis ratio was not fitted. Instead, the 2MASS photometric axis ratio of 0.9 was assumed. For this galaxy, the signal-to-noise was too low for the accurate measurement of the h_3 and h_4 moments. These were therefore suppressed during kinematic analysis using the pPXF code (Section 3). However, we note the significant h_3 detection in the re-analysis of the Spolaor et al. (2008a) data (Appendix A). Our data sampled only one data point within $1 R_e$. Radial binning was therefore carried out in the bins $R < 1.5 R_e$ and $R > 1.5 R_e$. For some of the outermost points errors in velocity dispersion exceeded 100 km s^{-1} . These data were omitted from both plots and analysis.

Fig. 14 shows that V_{rot} is lower in the outer radial range than in the inner range. There is also the suggestion of a falling σ with radius. The data were not fitted for rotation axis ratio due to low signal-to-noise and the large uncertainties in fits in axis ratio measurements when the value approaches 1.0. However, it is clear from the plot of V_{obs} with PA that the rotation has very low ellipticity (rotation axis ratio ≈ 1.0), similar to the 2MASS photometric axis ratio of 0.90. This value was therefore assumed for the rolling fits.

Due to the small sample size, rolling fits were performed to V_{obs} using 7 points in the inner region rising to 12 in the outer regions. The resultant plots with radius (Fig. 15) confirm the conclusions drawn from the plot with PA of a falling V_{rot} and σ with radius. Indeed, this galaxy shows the sharpest fall-off in σ with radius in our sample – falling from $> 300 \text{ km s}^{-1}$ in the centre to $\approx 100 \text{ km s}^{-1}$ at $1.5 R_e$, but

remaining near constant beyond. However, there appears to be a significant unexplained offset between σ from this work and the values from the data of Spolaor et al. (2008a) in the overlap region (both before and after the re-measurement of the data using the pPXF; See Appendix A). It is important to note that this discrepancy increases with decreasing radius, with the discrepancy rising from $\approx 20 \text{ km s}^{-1}$ at $1.4 R_e$ to 60 km s^{-1} at $1 R_e$ (see also Fig. 5). This clearly indicates that this is not a signal-to-noise issue. A detailed examination of the spectra of the two studies of NGC 1400 could identify no obvious reasons for such a discrepancy. Consequently, we must contemplate the possibility that this is a real effect. We therefore note that the sense of the discrepancy is consistent with the idea that the optical and NIR probe different stellar populations, with the NIR being dominated by a lower velocity dispersion (more centrally concentrated) population than the optical. The strong stellar population metallicity gradient in NGC 1400 ($\approx 0.38 \text{ dex/dex}$; Spolaor et al. 2008b) may therefore be the cause of the large discrepancy in this galaxy. The reconstructed 2-D velocity map of this galaxy is shown in Fig. 11.

PA_{kin} shows no significant variation with radius and is in good agreement with the photometric PA of 2MASS and Spitzer et al. (2009; in prep).

With regard to this galaxy’s rather uncertain morphological classification, the evidence for a disc with a declining rotation, but near constant profile would seem to favour its classification as an elliptical with an embedded disc.

4.5 NGC 821

NGC 821 is an isolated (Reda et al. 2007), elliptical galaxy with morphological classification E6. The galaxy is con-

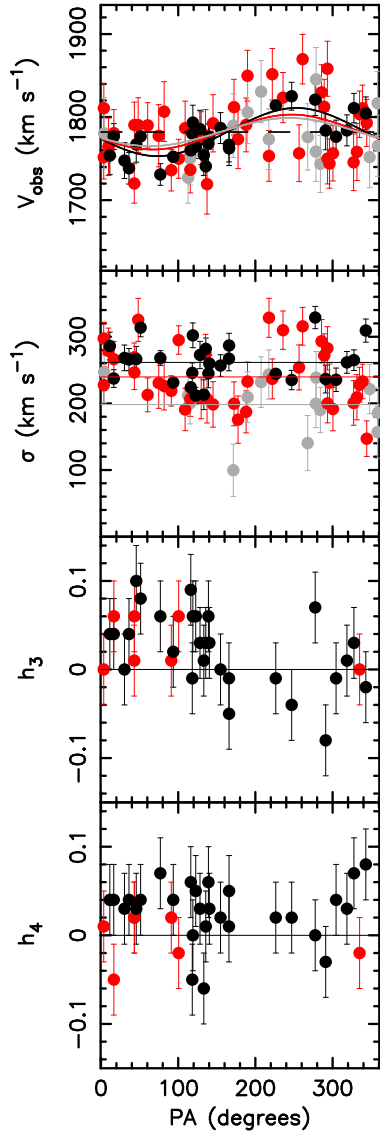


Figure 12. NGC 1407. Same as Fig. 6 except that the rotation axis ratio was not fitted but assumed to be equal to the 2MASS photometric axis ratio (i.e. 0.95). The major axis PA is 60° .

considered to possess a disk embedded in a spheroidal halo (Michard & Marchal 1994; Ravindranath et al. 2002; Emmersellam et al. 2004). The photometric profiles of Goudfrooij et al. (1994) show that ellipticity peaks around 15 arcsec ($0.3 R_e$). Kinematic profiles have been widely published (e.g. Pinkney et al. 2003; Proctor et al. 2005; Forestell & Gebhardt 2008), although there is still some debate as to whether the profile is falling or not and whether NGC 821 contains dark matter (Romanowsky et al. 2003). The stellar population study of Proctor et al. (2005) reveals a young central stellar population which gives way to old ages by 1 effective radius.

Plots of velocity moments with PA are shown in Fig. 16. Only the data within $1 R_e$ were fitted for position angle and rotation axis ratio due to low signal-to-noise and small sample size in the outer regions. The values derived from the inner regions was then assumed for the outer regions.

Fig. 16 shows strong rotation within $1 R_e$, but exhibits

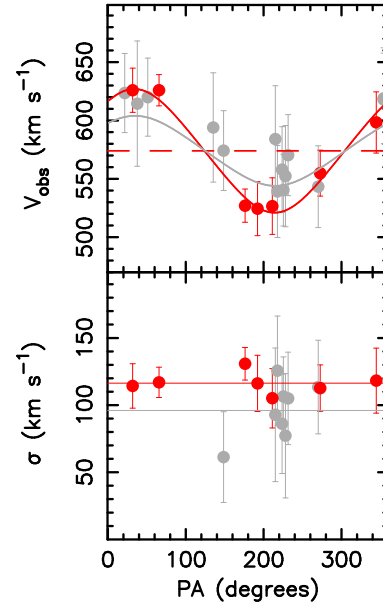


Figure 14. NGC 1400. Same as Fig. 6 with the following exceptions. The velocity moments h_3 and h_4 were suppressed in this low signal-to-noise sample. Radial bins of the independent data points are $R < 1.5 R_e$ and $R > 1.5 R_e$. The rotation axis ratio was not fitted but assumed to be 0.9 (i.e. equal to the 2MASS photometric axis ratio).

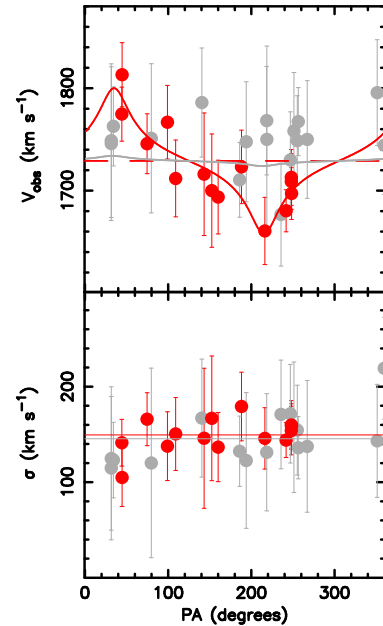


Figure 16. NGC 821. Same as Fig. 14 except that the radial binning is in ranges of $R < 1.0 R_e$ and $R > 1.0 R_e$ only. The major axis PA is 30° .

a value consistent with zero rotation beyond this region. We also detect no variation in σ with radius.

Rolling fits of the rotation velocity data (Fig. 17) were performed using 7 data points in the inner region rising to 12 data points in the outer regions of the galaxy. Fig. 17 confirms the falling V_{rot} with radius and also identified in the plots with PA. The figure also shows that, where they

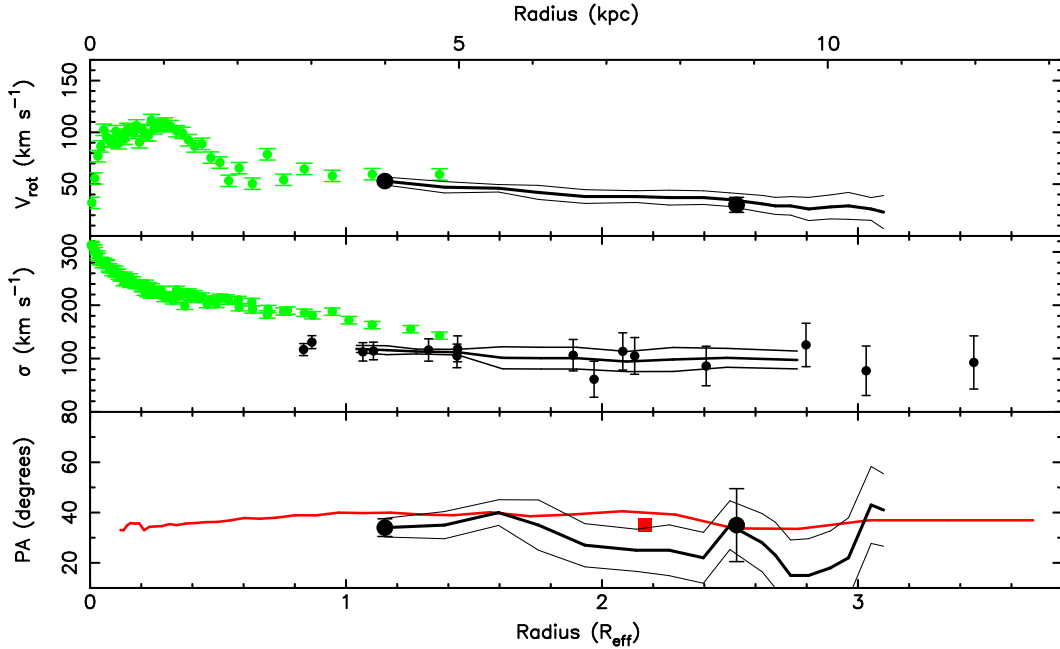


Figure 15. NGC 1400. Same as Fig. 7 with the following exceptions. The independent data points are for $R < 1.5 R_e$ and $R > 1.5 R_e$. Green data points in V_{rot} and σ plots are from the re-measurement of the data of Spolaor et al. (2008a) (see Appendix A). The red line in the PA plot is the Sloan i-band data of Spitzer et al. (2009; in prep).

overlap, there is good agreement between our results and both the (Em sellen et al. 2004) and Forestell & Gebhardt (2008) results for V_{rot} , σ , PA_{kin} and kinematic axis ratio, although we note one discrepant data point of Forestell & Gebhardt at $1.8 R_e$.

Our values are also in good agreement with literature studies of both stellar and planetary nebulae kinematics. We note that Coccato et al. (2009) also measure a planetary nebula rotation velocity consistent with zero for a data point at $5 R_e$ with rotation and σ of 14.25 km s^{-1} and 51.18 km s^{-1} , respectively.

The single kinematic axis ratio value that we derive is significantly lower than the photometric axis ratio, confirming the result found using the SAURON data (Krajinovic 2008).

It is also interesting to note that the extent of the disc evident in the V_{rot} plot of Fig. 17 is similar to the extent of both the dip in photometric axis ratio of Goudfrooij et al. (1994) (bottom plot; Fig. 17) and to the extent of the young central population identified in Proctor et al. (2005), both of which are evident out to nearly $1 R_e$. This lends credence to the speculation that the young central ages are associated with the presence of a disc that has undergone a recent burst of star formation. Also of interest is the fact that the photometric axis ratio of the galaxy remains fairly low (~ 0.7) even at radii well beyond the extent of the disc. This suggests that the galaxy is comprised of a disc embedded in an highly elliptical bulge in agreement with the photometric classification in the literature (Michard & Marchal 1994; Ravindranath et al. 2002; Em sellen et al. 2004).

To aid in the visualisation of our results, and to facilitate the comparison of our results with those of SAURON (Em sellen et al. 2004), we have reconstructed the 2-D rotation map of the galaxy in Fig. 18. The image was generated

using the rolling σ values of V_{rot} of Fig. 17 and assuming rotation to have constant PA_{kin} and axis ratio, with values equal to the values within $1 R_e$ (33 and 0.3 respectively; Table 4). The SAURON map is also shown. Despite the spatial gap between the two data sets, agreement can be seen to be good.

5 DISCUSSION

We have demonstrated that our analysis gives good agreement with the SAURON (Em sellen et al. 2004) study and other data from the literature in regions where they overlap. We have also shown that the results provide valuable insights into individual galaxies. We next consider our results in a more general sense.

5.1 Rotation

The five galaxies in our sample exhibit a range of rotation profiles. Two galaxies (NGC 1407 and NGC 4494) exhibit flat rotation profiles (within errors) beyond 0.2 and $0.4 R_e$ respectively. One galaxy (NGC 2768) exhibits rotation that increases in amplitude over the full extent of our data (i.e. to $3 R_e$). The remaining two galaxies (NGC 821 and NGC 1400) exhibit rotation curves that decline beyond $1 R_e$, and in the case of NGC 821, becomes consistent with zero rotation by $1.5 R_e$. It is therefore evident from our data that studies confined to the central regions of galaxies can miss vital aspects of their rotation properties.

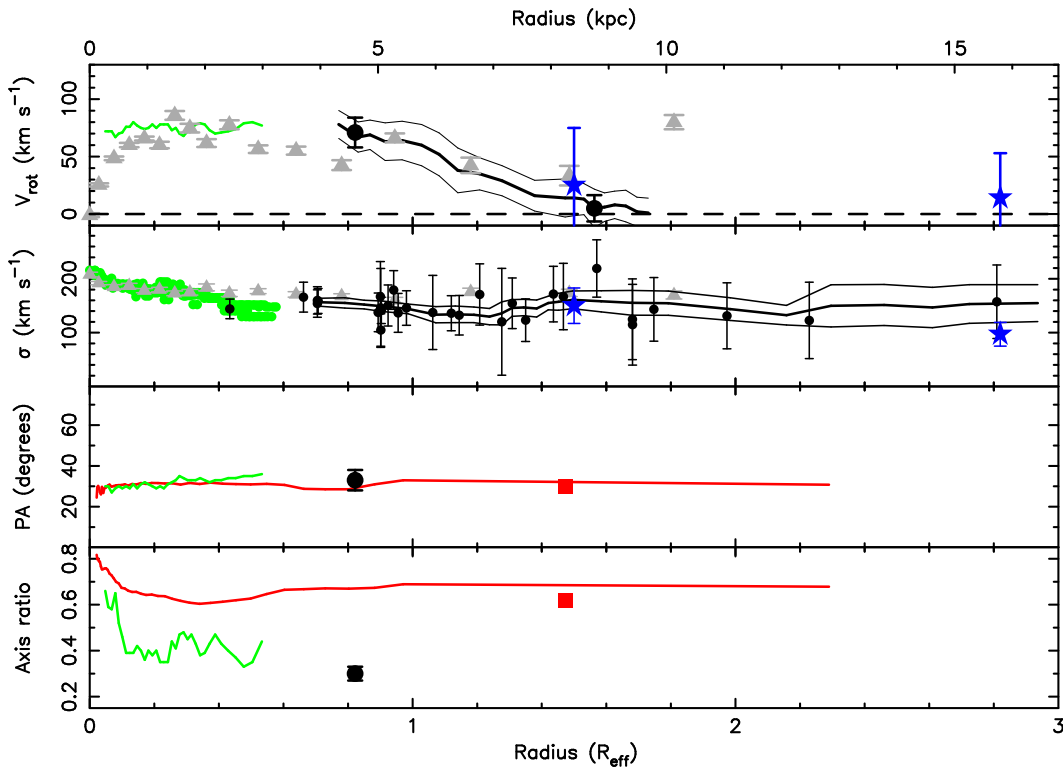


Figure 17. NGC 821. Same as Fig. 7 with the following exceptions. Radial binning is in ranges of $R < 1.0 R_e$ and $R > 1.0 R_e$ only. Kinematic PA and axis ratio were only estimated for the inner range. Inner range values of these parameters were assumed for the measurement of V_{rot} . Green data points are from SAURON (Em slem et al. 2004). Grey data points are from Forestell & Gebhardt (2008). Blue stars are the planetary nebula data of Cocato et al. (2009). Red lines in PA and axis ratio plots are the photometric data of Goudfrooij et al. (1994).

5.2 Velocity dispersion

The *ve* galaxies in our sample exhibit only shallow slopes in σ with radius beyond $1 R_e$. Indeed, in most cases, results in these regions are consistent with zero slope at the 2σ significance level. Such flat and rotation profiles (with the possible exception of NGC 821) represent the classic signature of a dark matter halo in each galaxy. These data will therefore prove invaluable to future studies that perform full dynamical modeling of galaxies.

5.3 Higher order moments

We note that all 5 galaxies in this study exhibit non-zero h_3 values, the sense of which mirror the rotation velocity. This trend is identified in the NIR spectra of this work in 3 of the 5 galaxies. In NGC 1400 it is identified in the re-analysis of the Spolaor et al. (2008a) optical data, while in NGC 821 it is evident in the optical data of Forestell & Gebhardt (2008). When h_3 follows the inverse trend of the rotation velocity it is often taken as the signature of a cold (rotating) stellar population embedded within a hotter (pressure supported) system. However, Balcells (1991) shows that this signature can also be induced by the action of a merger event. We therefore conclude that all *ve* of the observed galaxies are either merger remnants or harbour embedded discs.

There do not appear to be any clear trends in the h_4 parameter in our current data. We suspect that this is due to the low signal-to-noise of the majority of our data.

5.4 Kinematic and photometric misalignment

For fast-rotators, the SAURON survey revealed that the kinematic and photometric position angles are usually well aligned, and that their axis ratios are similar (Em slem et al. 2007). This is true for two of our galaxies (NGC 2768 and NGC 1400). However, in both NGC 4494 and NGC 821 there appear to be significant offsets between kinematic and photometric axis ratios, while for NGC 821 an offset in axis ratio is detected. This result for NGC 821 confirms the SAURON result, despite the fact that we have only one kinematic data point at large radii.

5.5 Anisotropy diagram

Binney (1978) showed the usefulness of the anisotropy diagram (V/σ vs photometric ellipticity) as applied to elliptical galaxies. In Fig. 19 we show this diagram for the two galaxies in common with the SAURON survey (i.e. NGC 821 and NGC 2768), with the lines indicating the radial variation. The plot shows that the value of V/σ in NGC 821 declines with increasing radius, while NGC 2768 increases. Thus NGC 821 trends away from the isotropic rotator line, while NGC 2768 trends towards it. It is therefore clear that the central regions of galaxies do not necessarily reflect the properties of galaxies as a whole, and care must be taken when drawing conclusions from central data only. We note that similar conclusions were reached from PN kinematics by Cocato et al. (2009).

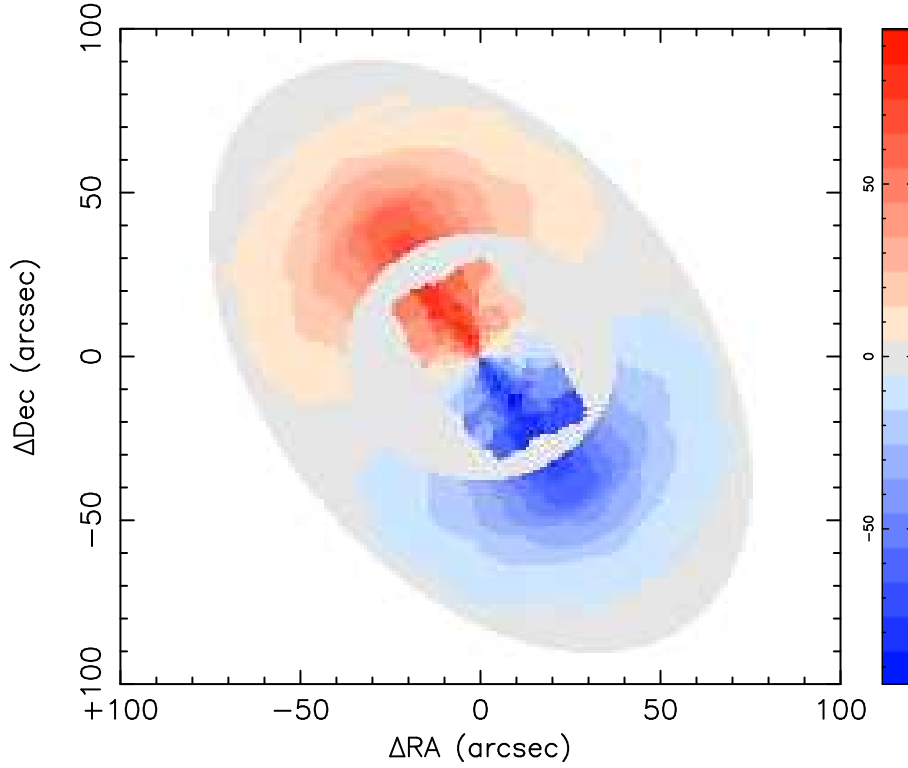


Figure 18. NGC 821. Reconstruction of the rotation profile using the rolling fits of V_{rot} (Fig. 17). However, beyond $1 R_e$ the values of kinematic PA and axis ratio are assumed to be the same as within $1 R_e$ (33 and 0.3 respectively). The outer boundary of the map has been chosen to reflect the photometric axis ratio of the galaxy (0.62). The colour scale (in km s^{-1}) is shown on the right. Also shown is the SAURON (Em sellen et al. 2004) map of the central regions of the galaxy. The agreement between the data sets is again extremely good.

5.6 The SAURON R parameter

As part of the analysis of the SAURON 2-D kinematics, Em sellen et al. (2007) defined a new parameter, R as;

$$R = \frac{\langle R : j \rangle}{\langle R : \sqrt{V^2 + \sigma^2} \rangle}; \quad (3)$$

where $\langle R : j \rangle$ is the luminosity weighted average of the product of radius and rotation velocity over the surface of the map and $\langle R : \sqrt{V^2 + \sigma^2} \rangle$ is a similarly luminosity weighted average. Thus R is a measure of the projected angular momentum per unit mass (i.e. the specific angular momentum).

Em sellen et al. (2007) found that galaxies were clearly distinguished into two classes on the basis of this parameter, i.e. ‘fast-rotators’ ($R > 0.1$) and ‘slow-rotators’ ($R < 0.1$). Fast rotators tended to be lower luminosity, discy ellipticals, while the massive boxy ellipticals were often slow rotators.

The two galaxies in common with the SAURON project (NGC 821 and NGC 2768) were both classified as ‘fast-rotators’ (i.e. $R > 0.1$) by Em sellen et al. (2007). Their R values are very similar (0.258 and 0.268 respectively). However, we find that when probed to radii greater than $1 R_e$ NGC 821 reveals a declining rotation velocity (and roughly constant velocity dispersion) profile. This suggests that if the outer region data were included the calculated R value would be smaller. Although due to the luminosity weighting in the R definition more emphasis is given to the

central regions, so the actual change in the value might be small.

To test this, we constructed a model of each of these galaxies. Each model assumed $R^{1=4}$ de Vaucouleur’s profiles. For each galaxy, the rotation parameters (V_{rot} , PA_{kin} and kinematic axis ratio) were then characterised by a polynomial fit to the plots with radius (Figures 7 and 17). The luminosity and velocity maps so produced were then combined as per Em sellen et al. (2007) to calculate the R values inside ellipses of increasing effective radius². The results are presented in Fig. 20. Agreement with the published SAURON values for the inner regions can be seen to be extremely good. However, for NGC 821 our model suggests that, despite its classification as a fast-rotator (when only data from within $1 R_e$ is considered), the decreasing rotation at large radii could indeed result in the galaxy being classified as a slow-rotator when all the data out to $3 R_e$ are considered.

In contrast to NGC 821, NGC 2768 has a profile that continues to rise all the way out to $3 R_e$. Its R value will therefore continue to increase as larger and larger radii are included in the calculation, and the galaxy will remain a ‘fast-rotator’. Therefore, despite their similarity within one effective radius, both of these galaxies have vastly different

² Although precise values of the sersic index for the two galaxies are not available, we note that the results are relatively insensitive to this parameter

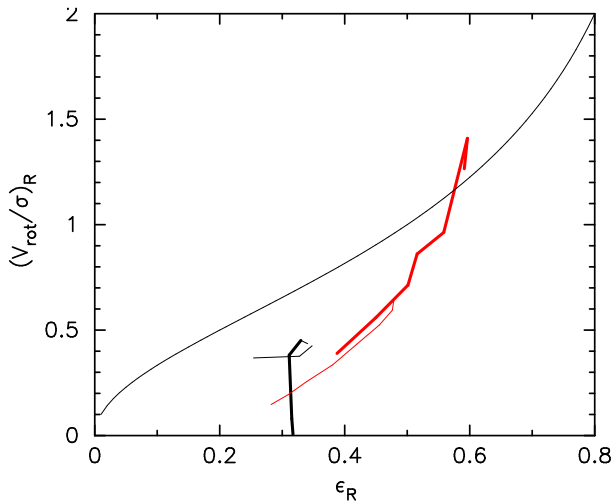


Figure 19. Anisotropy diagram. V_{rot}/σ is plotted against ellipticity at various radii for NGC 821 (black) and NGC 2768 (red). The remaining three galaxies are not shown as their V_{rot}/σ and photometric ellipticities show little or no variation with radius. The thin lines represent the inner SAURON data, and the thick lines are our data out to $3 R_e$. The smooth curved line represents an ideal isotropic rotator.

distributions of angular momentum with radius (see also Coccato et al. 2009).

Although not observed in the SAURON survey, we assume NGC 1407 to be a slow-rotator, as its V/σ value is low (we estimate 0.09 on the basis of Equation 23 of Cappellari et al. 2007) and its kinematics are similar to NGC 5982 which was observed by SAURON (Krajkovic et al. 2008) and defined as a slow-rotator (Emmelmann et al. 2007). In the case of NGC 1400 and NGC 4494 their relatively high rotation velocities and relatively low velocity dispersions clearly indicate them to be fast rotators.

5.7 The RMS velocity parameter

In addition to the V_{rot}/σ and λ_R parameters which probe orbital anisotropy and angular momentum respectively, another fundamental parameter of a galaxy is its internal kinetic energy. The observational measure of the total kinetic energy is the RMS velocity parameter, which locally is equal to the quadrature combination of rotation and dispersion velocities, i.e. $V_{\text{rms}} = \sqrt{V_{\text{rot}}^2 + \sigma^2}$ (e.g. Napolitano et al. 2009).

In Fig. 21 we show the RMS velocity parameter as a function of major axis radius for the five galaxies in our sample. We show the inner regions from literature data and the outer regions from our data. For all but one galaxy (NGC 2768) a general decline in the RMS velocity parameter is seen with radius (as might be expected from the generally flat rotation velocity and declining velocity dispersion profiles observed). The implications of this for the mass profile of each galaxy requires detailed dynamical modeling.

6 CONCLUSIONS

We have developed a new technique for extracting spectra of the galaxy background contained in the multi-object obser-

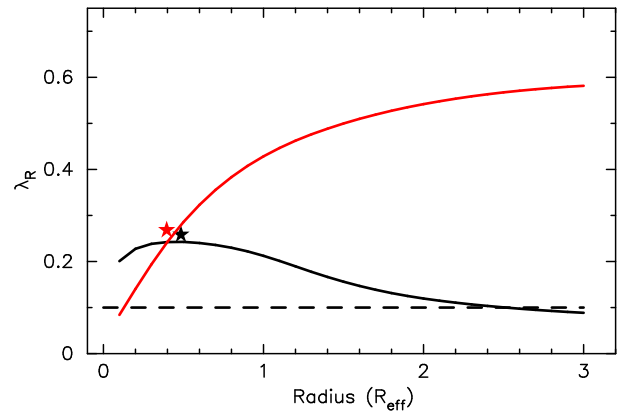


Figure 20. The λ_R parameter (cumulative value of λ within radius R) with major axis radius scaled by the effective radius. The SAURON central values are presented as stars, and our data by solid lines. Here NGC 821 is black and NGC 2768 is red. The dashed line represents the delimiting value of 0.1 between ‘fast-’ and ‘slow-’ rotators (as defined in Emmelmann et al. 2007). While both galaxies are classified as fast-rotators based on SAURON data within $1 R_e$, NGC 821 would be classified as a slow-rotator if the data to $3 R_e$ are considered.

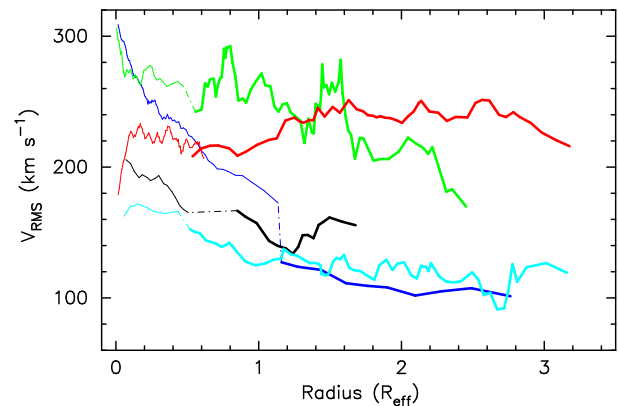


Figure 21. V_{rms} parameter with major axis radius. Galaxies are colour coded, i.e. NGC 821 black, NGC 1400 blue, NGC 1407 green, NGC 2768 red and NGC 4494 cyan. The thin lines represent the inner literature data, and the thick lines are our data out to larger radii (with extrapolated dashed lines connecting the two). In general the V_{rms} profiles decline with radius.

ervations using the DEIMOS spectrograph on the Keck telescope. Here, the slits contained globular clusters, which were the primary target of the observing programme. The technique allows measurement of the velocity moments (rotation velocity, velocity dispersion, and Gauss-Hermite coefficients h_3 and h_4) in a galaxy halo out to at least $3 R_e$, covering a surface area of some $24 R_e^2$, in comparison to the $0.4 R_e^2$ achieved by the SAURON integral field unit.

For the 5 early-type galaxies in our sample, we have demonstrated that the agreement between our results and the literature values is generally extremely good in the regions of overlap, including the velocity dispersion profiles from planetary nebulae data for NGC 821 and NGC 4494.

For NGC 821 we show that the kinematic signature of the disc identified in the surface photometry disappears at

around $1.5 R_e$, while the photometry remains highly elliptical in the outer regions. From this we conclude that NGC 821 constitutes a highly elliptical bulge with an embedded central disc. For NGC 1400, we also detect a falling rotation profile beyond $1 R_e$. When considered in conjunction with the significant h_3 found by Spolaor et al. (2008a) in the inner regions, this suggests that this early-type galaxy also contains an embedded disc. For both NGC 1407 and NGC 4494, which are currently classified as pure elliptical galaxies, the detection of a trend in the Gaussian Hermite h_3 coefficient suggests that these too harbour a sub-population with 'disk-like' kinematics. In NGC 4494, both the 'disk-like' kinematics and a coordinated shift in photometric and kinematic position angles provide strong support for the idea that this galaxy is a merger remnant. The kinematics of NGC 2768 clearly indicates that a disc is present. However, in this case, the disc becomes more prominent with galactocentric radius, suggest that this galaxy is, in fact, an S0. It is therefore apparent that all the galaxies in our sample show evidence for a disc or disc-like components.

We estimate the angular momentum parameter λ used in the SAURON survey to classify early-type galaxies as either fast or slow rotators. Importantly, our analysis shows that the central kinematics are not necessarily representative of the kinematics at larger radii, and that galaxies can change their rotator class when data from larger radii are considered. This has important repercussions for any attempts to classify galaxies by their central kinematic properties alone.

We have shown that our sample galaxies reveal the relatively flat rotation and velocity dispersion profiles suggestive of massive dark matter halos, thus demonstrating the value that our new technique will have when full dynamical modelling of these galaxies is carried out.

Finally, we note that the observations used here were not optimised for this project. Future work that uses slit masks designed for the purpose of extracting galaxy halo spectra should provide additional improvements.

References

- Balcells M., 1991, *A & A*, 249, L9
 Bender R., 1988, *A & A*, 193, L7
 Bender R., 1990, *A & A*, 229, 441
 Bender R., Saglia R. P., Gerhard O. E., 1994, *MNRAS* 269, 785
 Binney J., 1978, *MNRAS*, 183, 501
 Cappellari M., Emsellem E., 2004, *PASP*, 116, 138
 Cappellari M., et al., 2007, *MNRAS*, 379, 418
 Carollo, C. M., Franx M., Illingworth G. D., Forbes D. A., 1997, *ApJ*, 481, 710
 Cocato et al., 2009, *MNRAS*, in press
 Da Costa L. N., et al., 1998, *AJ*, 116, 1
 Dekel A., Stoehr F., Mamon G. A., Cox T. J., Novak G. S., Primack J. R., 2005, *Nature*, 437, 707
 Denicolò G., Terlevich R., Terlevich E., Forbes D. A., Terlevich A., 2005, *MNRAS*, 358, 813
 de Vaucouleurs G., 1953, *MNRAS*, 113, 134
 de Vaucouleurs G., de Vaucouleurs A., Corwin H. G., Buta R. J., Paturel G., Fouque P., 1991, *Third Reference Catalogue of Bright Galaxies (RC3)*. Springer-Verlag, Berlin, Heidelberg, New York
 Emsellem E., et al., 2004, *MNRAS*, 352, 721
 Emsellem E., et al., 2007, *MNRAS*, 379, 401
 Filippenko A. V., Chomock R., 2000, *IAUC*, 7511, 2
 Forbes D. A., Franx M., Illingworth G. D., Carollo C. M., 1996, *ApJ*, 467, 126
 Forestell A., Gebhardt K., 2008, *arXiv:0803.3626*
 Fried D. L., Illingworth G. D., 1994, *AJ*, 107, 992
 Gerhard O. E., 1993, *MNRAS*, 265, 213
 Goudfrooij P., Hansen L., Jørgensen H. E., Nørgaard-Nielsen H. U., de Jong T., van den Hoek L. B., 1994, *A & S*, 104, 179
 Graham A. W., Colless M. M., Busarello G., Zaggia S., Longo G., 1998, *A & S*, 133, 325
 Hakobyan A. A., Petrosian A. R., McLean B., Kunth D., Allen R. J., Turatto M., Barbon R., 2008, *A & A*, 488, 523
 Howell J. H., 2005, *AJ*, 130, 2065
 Jarrett T. H., Chester T., Cutri R., Schneider S., Skrutskie M., Huchra J. P., 2000, *AJ*, 119, 2498
 Jarrett T. H., Chester T., Cutri R., Schneider S. E., Huchra J. P., 2003, *AJ*, 125, 525
 Kronawitter A., Saglia R. P., Gerhard O., Bender R., 2000, *A & S*, 144, 53
 Krajnovic D., Cappellari M., de Zeeuw P. T., Copin Y., 2006, *MNRAS*, 366, 787
 Krajnovic D., et al., 2008, *MNRAS*, 390, 93
 Lauer T. R., et al., 1995, *AJ*, 110, 2622
 Longo G., Zaggia S. R., Busarello G., Richter G., 1994, *A & S*, 105, 433
 Mamon G. A., Lokas E. L., 2005, *MNRAS*, 363, 705
 Martel A. R., et al., 2004, *AJ*, 128, 2758
 McDermid R. M., et al., 2006, *MNRAS*, 373, 906
 McMillan P. J., Athanassoula E., Dehnen W., 2007, *MNRAS*, 376, 1261
 Mehlert D., Saglia R. P., Bender R., Wegner G., 2000, *A & S*, 141, 449
 Michard R., Archal J., 1994, *A & S*, 105, 481
 Napolitano N. R., et al., 2009, *MNRAS*, 393, 329
 Norris M. A., et al., 2008, *MNRAS*, 385, 40
 Peletier R. F., Davies R. L., Illingworth G. D., Davis L. E.,

Cawson M., 1990, *AJ*, 100, 1091
 Pinkney J., et al., 2003, *ApJ*, 596, 903
 Proctor R. N., Forbes D. A., Forestella., Gebhardt K., 2005, *MNRAS*, 362, 857
 Proctor R. N., Forbes D. A., Brodie J. P., Strader J., 2008, *MNRAS*, 385, 1709
 Ravindranath S., Holc., Filippenko A. V., 2002, *ApJ*, 566, 801
 Reda F. M., Proctor R. N., Forbes D. A., Haug K. T., Larsen S. S., 2007, *MNRAS*, 377, 1772
 Rix H-W., White S. D. M., 1992, *MNRAS*, 254, 389
 Románowsky A. J., et al., 2003, *Science*, 301, 1696
 Románowsky A. J., Strader J., Spitler L., Johnson R., Brodie J. P., Forbes D. A., Ponomarev T., 2008, *ApJ*, in press
 Saglia R. P., 1993, *ApJ*, 403, 567
 Sanchez-Balazquez P., Gorgas J., Cardiel N., 2006, *A&A*, 457, 823
 Sandage A., Tamman G. A., van den Bergh S., 1981, *JRAS*, 75, 267
 Sandage A., Bedke J., 1994, *The Carnegie Atlas of Galaxies*. Carnegie Institution of Washington with The Flintridge Foundation, Washington, DC
 Silchenko O., 2006, *ApJ*, 641, 229
 Simkin S. M., 1974, *A&A*, 31, 129
 Spolaor M., Forbes D. A., Haug K. T., Proctor R. N., Brough S., 2008a, *MNRAS*, 385, 667
 Spolaor M., Forbes D. A., Proctor R. N., Haug K. T., Brough S., 2008b, *MNRAS*, 385, 675
 Statler T. S., Smecker-Hane T., 1999, *AJ*, 117, 839
 Thomas J., Jesseit R., Naab T., Saglia R. P., Burkert A., Bender R., 2007, *MNRAS*, 381, 1672
 Trentham N., Tully R. B., Madaia A., 2006, *MNRAS*, 369, 1375
 van der Marel R. P., 1994, *MNRAS*, 270, 271
 van der Marel R. P., Franx, M., 1993, *ApJ*, 407, 525
 Weiland M. L., Hemquist L., 1996, *ApJ*, 460, 101

Acknowledgements

The analysis pipeline used in this work to reduce the DEIMOS data was developed at UC Berkeley with support from NSF grant AST-0071048. We also use the excellent Penalized Pixel-Fitting method (pPXF) code developed by Cappellari & Emsellem (2004) and the data products from the Two Micron All Sky Survey (2MASS), which is a joint project of the University of Massachusetts and the Infrared Processing and Analysis Center/California Institute of Technology, funded by the National Aeronautics and Space Administration and the National Science Foundation. The authors acknowledge the data analysis facilities provided by IRAF, which is distributed by the National Optical Astronomy Observatories and operated by AURA, Inc., under cooperative agreement with the National Science Foundation. This work was supported by the National Science Foundation under Grants AST-0507729 and AST-0808099. J.S. was supported by NASA through a Hubble Fellowship, administered by the Space Telescope Science Institute, which is operated by the Association of Universities for Research in Astronomy, Incorporated, under NASA contract NAS5-26555. Finally, we also thank the Australian Research Council for funding that supported this work.

Parameter	New value		Old value	
NGC 1400				
V_{sys}	563	5	560	10
V_{rot}	113	6	139	17
σ	281	7	301	4
NGC 1407				
V_{sys}	1791	5	1794	10
V_{rot}	54	6	53	19
σ	270	7	313	9

Table A 1. New and old (Spolaor et al. 2008a) kinematic parameters for NGC 1400 and NGC 1407.

APPENDIX A: THE RE-ANALYSIS OF NGC 1400 AND NGC 1407 LONG-SLIT DATA.

Spolaor et al. (2008a) used the van der Marel & Franx (1993) code to measure velocity moments in 68 and 82 apertures along the major axes for NGC 1407 and NGC 1400, respectively. The spectra had a S/N of $\sim 30 \text{ \AA}^{-1}$ at 5000 \AA , and reached a radial extent of $0.56 R_e$ ($\sim 4.11 \text{ kpc}$) for NGC 1407 and $1.30 R_e$ ($\sim 3.58 \text{ kpc}$) for NGC 1400. Measurement of moments was then carried out using 17 template stars of spectral class F5 to K4. Briefly, the procedure identified the template that best fit the central regions (where the signal-to-noise is highest) and applied this to all spatial slices. The drawback to this method is that the best-fitting template was found using only the very central regions and the existence of strong stellar population gradients (particularly metallicity) may require differing templates in the inner and outer regions.

We have therefore re-analysed the data of Spolaor et al. (2008a) using the pPXF code of Cappellari et al. (2007). The main advantage of this code is that:

- i) A template match is found for all individual spatial slices.
- ii) The code finds the combination of templates that best matches the data, further improving the fit.

The results of the new fits are shown in Fig. A1 and Table A1. Errors on derived parameters were estimated by running a series of Monte Carlo simulations. The results do not change the general conclusions of Spolaor et al. (2008a). However, the kinematically decoupled core identified in Spolaor et al. (2008a) is now much more distinct and the h_3 and h_4 values appear much more consistent.

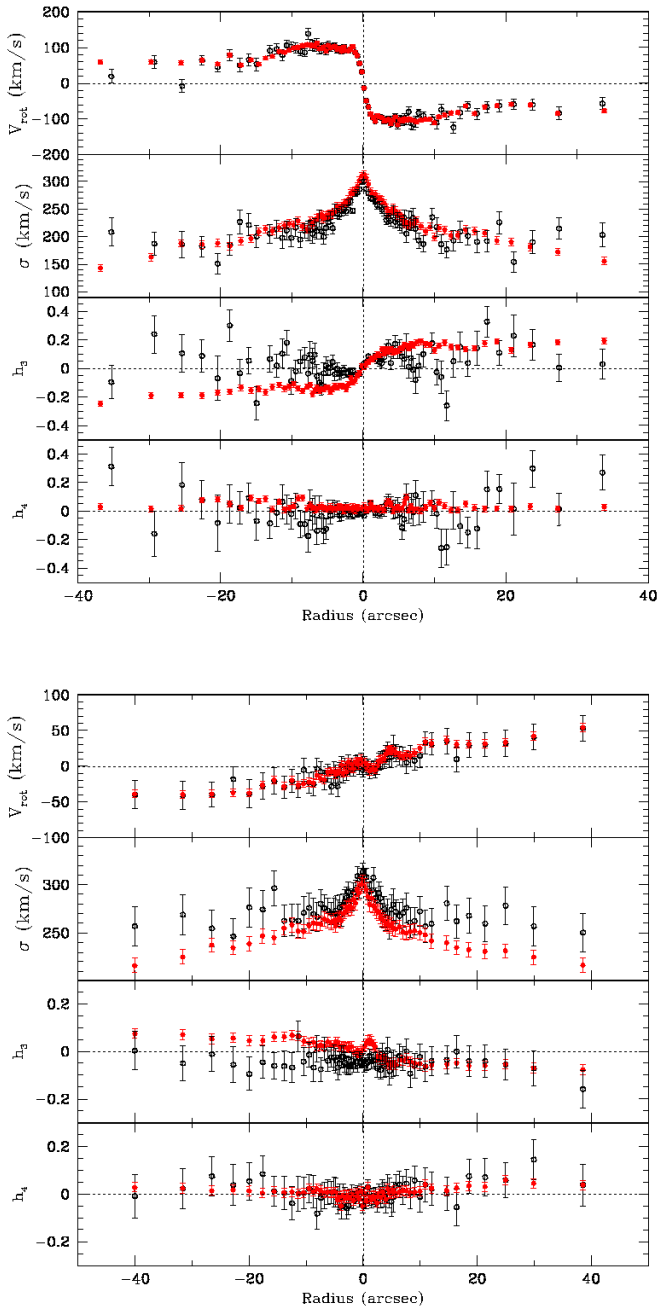


Figure A 1. A comparison of the results of the results of Spolaor et al. (2008a) (black points; NGC 1400; top and NGC 1407; bottom) to our re-analysis using the pPXF software (red points).